九州大学学術情報リポジトリ
Kyushu University Institutional Repository

Nonlinear Simulation of Plasma Blob Formation and Radial Propagation in the Scrape-off Layer

Sugita, Satoru
Interdisciplinary Graduate School of Engineering Sciences, Kyushu University

Yagi, Masatoshi
Research Institute for Applied Mechanics, Kyushu University

Ito, Sanae-I.
Research Institute for Applied Mechanics, Kyushu University

https://doi.org/10.15017/27046

出版情報：九州大学応用力学研究所所報. 136, pp.1-18, 2009-03. Research Institute for Applied Mechanics, Kyushu University
バージョン：
権利関係：

Nonlinear Simulation of Plasma Blob Formation and Radial Propagation in the Scrape-off Layer

Satoru SUGITA*1, Masatoshi YAGI*2 and Sanae-I. ITOH*2
E-mail of corresponding author: *satoru@riam.kyushu-u.ac.jp*

(Received January 30, 2009)

Abstract

The nonlinear fluid simulation of the isolated plasma blob propagation and interchange turbulence in the scrape-off layer are demonstrated using 2-dimensional Hasegawa-Wakatani equation. In the propagation process of the isolated blob, density nonlinear term in the model equation has the strong effect on the dynamics of blob propagation. Interchange turbulence in the scrape-off layer is reproduced by the collapse and spread of the plasma blob which is formed by the Rayleigh-Taylor finger detached at the separatrix.

Key words : *scrape-off layer, second SOL, plasma blob, Kelvin-Helmholtz instability, interchange instability, non-diffusive turbulent transport*

1. Introduction

The turbulent transport of a Tokamak edge plasma has been investigated by many researchers[1]. Recent experimental results show that the transport in this region, rather than being dominated by diffusive process, is mostly convective and intermittent[1]. The region where the density profile is deviated from the exponential profile predicted by the diffusion process is known as 2nd SOL (see Fig. 1). Particles which cross the separatrix and enter the scrape-off layer (SOL) with its open field lines are normally expected to follow the field lines to the divertor chamber. However, if the radial convection rate is fast enough, as it is to experimentally observed, particles can recycle at the main chamber wall instead, reducing the divertor efficiency. Rapid convective transport of the SOL plasma to the main chamber wall possibly contributes to increased impurity level and to observed density limit. The most abundant experimental indication of the rapid radial convective transport are from measurement of magnetic-field-aligned plasma filaments, referred to as "blobs", in the SOL[3–7]. Thus, the research on the blob transport is a crucial issue for the development of a thermonuclear fusion reactor, like International Thermonuclear Experimental Reactor (ITER).

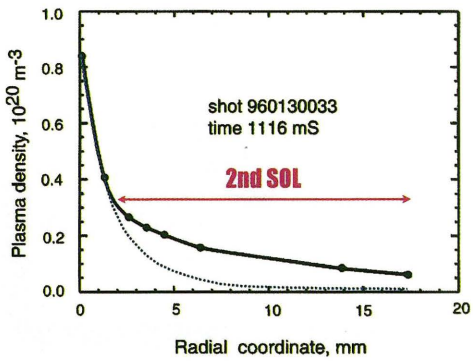

Fig. 1 Typical experimental plasma density profile in Alcator C-Mod. The blue dotted line is the normal exponential decay diffusion. (Ref. [2])

The plasma blob transport is explained based on the formation and propagation of long-lived macroscopic coherent structures. So far, there does not appear to be a generally accepted mechanism of a blob formation, however, the clear picture of their dynamics and stability is drawn in a recent theoretical and computational studies[8–13]. The self-consistent treatment of the blob transport including their formation process is still open issue[14, 15].

In this thesis, we develop 2D simulation codes to ana-

*1 Interdisciplinary Graduate School of Engineering Sciences, Kyushu University
*2 Research Institute for Applied Mechanics, Kyushu University

lyze the SOL interchange turbulence and the blob transport using Hasegawa-Wakatani model equations[19]. We extend the 2D Hasegawa-Wakatani model which describes the blob dynamics in the SOL[8], such that it includes a density nonlinearity in the continuity equation and compare the simulation results with those of that.

The thesis is organized as follows: In Chapter 2, the background of blob transport in the SOL is reviewed, in Chapter3, model equations, numerical schemes and boundary conditions are explained and simulation results of the blob transport are shown. Then, effect of the density nonlinearity is discussed. In Chapter 4, nonlinear simulations of the SOL interchange turbulence are performed. The blob formation and its transport is investigated self-consistently. The summary and the discussion are given in Chapter 5.

2. Review

2.1 Radial Density Distribution in SOL

In this section, the radial density distribution in the SOL is explained from the view point of the particle balance. Fig. 2 shows the schematic diagram of the plasma flow from the confined plasma into the SOL. In

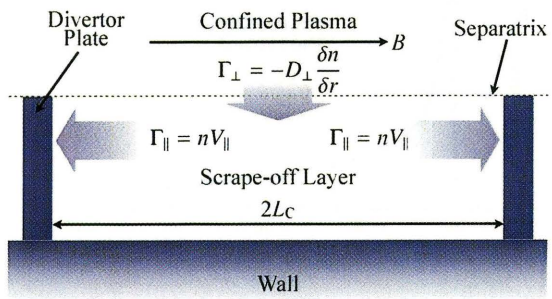

Fig. 2 Schematic diagram of the plasma flow from the confined plasma into the SOL by cross-field diffusion and along the field in the SOL to the divertor target.

the steady state, if there are no sources or skins (such as ionization) in the scrape-off layer, the loss along the field line from any given flux tube is balanced by the net flow across the field line into the flux tube:

$$-\frac{\mathrm{d}}{\mathrm{d}r}\left[D_\perp \frac{\mathrm{d}n}{\mathrm{d}r}\right] = \frac{nc_\mathrm{s}}{L_\mathrm{c}} \tag{1}$$

where $D_\perp$ is the cross-field diffusion coefficient, $c_\mathrm{s} = \sqrt{T_e/m_i}$ is the ion acoustic speed and L_c is the connection length along the flux tube to the flow stagnation point. With the assumption that $D_\perp$ and c_s are independent of radius, Eq. (1) is easily integrated to obtain

$$n(r) = n(a)\exp\left[-\frac{r-a}{\lambda_n}\right] \tag{2}$$

with

$$\lambda_n = \left(\frac{D_\perp L_\mathrm{c}}{c_\mathrm{s}}\right)^{1/2}, \tag{3}$$

where a is the minor radius at the separatrix, and λ_n is the electron density e-folding length, Eq. (3) shows that the radial density profile in the SOL plasma exponentially decays.

Similarly, a temperature profile is evaluated using the electron heat balance as:

$$T_e(r) = T_e(a)\exp\left[-\frac{r-a}{\lambda_T}\right] \tag{4}$$

with

$$1 + \frac{\lambda_n}{\lambda_T} = \frac{\delta}{5/2} + \frac{\chi_\perp \lambda_n}{D_\perp \lambda_{T_e}}, \tag{5}$$

where λ_T is the electron temperature e-folding length, and $\chi_\perp$ is the cross-field thermal diffusivity. Equations (2) and (4) give a radial distribution of n_e and T_e.

Equations (3) and (5) give the e-folding lengths in the scrape-off layer in terms of the cross-field transport coefficients. Experimentally, the measured values of λ_n and λ_T are used to deduce $D_\perp$ and $\chi_\perp$. Typical values are $\lambda \sim 10$mm. If there are no sources in the scrape-off layer, this measurement together with the assumption that $T_e = T_i$, gives the estimation of c_s and $D_\perp$. This is typically $D_\perp \sim 1\mathrm{m}^2\mathrm{sec}^{-1}$. Experimental results show that $D_\perp$ is inversely proportional to density. However, since density and temperature changes in the boundary region are correlated, this behaviour can also be interpreted as a temperature dependence of $D_\perp$. Absolute values of $D_\perp$ comparable with the Bohm diffusion coefficient, $D_\mathrm{B} = T/16eB$, are frequently obtained, although the scaling with T_e and B does not agree. If either particle or energy sources are present in the SOL then the calculation of transport coefficients is much more difficult.

It is possible to make rough estimates of the expected values of the density and temperature at the last closed flux surface (LCFS) by using global particle and energy balances. The integrated particle flux to the limiter must by equal to the total flux diffusing out from the confined plasma. A particle confinement time, τ_p, can be defined as

$$\Gamma_n = \frac{\bar{n}V}{\tau_\mathrm{p}} \tag{6}$$

where Γ_n is the total particle outflux, $\bar{n}$ is the average plasma density and V the plasma volume.

Using Eq. (2) the total flux to a single poloidal limiter is given by

$$\Gamma_\mathrm{L} = 4\pi a \int_a^\infty n(a)\exp\left[-\frac{r-a}{\lambda_n}\right] c_\mathrm{s}\,\mathrm{d}r. \tag{7}$$

Carrying out the integration in Eq. (7) and equating Γ_n to Γ_L, the edge density is given by

$$n(a) = \frac{\bar{n}V}{\tau_p}\frac{1}{4\pi a\lambda_n c_s}. \tag{8}$$

To estimate an upper bound of the edge temperature $T_e(a)$, all the power is assumed to be lost by particle flow across the sheath, without radiation. Such a calculation is only valid for limiter Tokamaks, The case of divertors is more complicated because much of the recycling takes place in the SOL near the target plates.

2.2 Blob Model

In this section, the blob model is briefly explained. The theoretical model for the plasma blob propagation is recently proposed by Krasheninnikov[16]. The basic mechanism behind the rapid convection appears to be the following: In general, any macroscopic clump of particles in a toroidal plasma would tend to be polarized due to species-dependent processes such as the ∇B and curvature drifts. In the core plasma with its closed flux surfaces, this charge separation is short-circuited by free-streaming electrons. In the SOL, however, a finite potential can be supported on the open fields due to sheath formation and its resistivity at the end points. A poloidal electric field thus formed, coupled with the toroidal magnetic field, then leads to a rapid $\mathbf{E}\times\mathbf{B}$ drift of the blob.

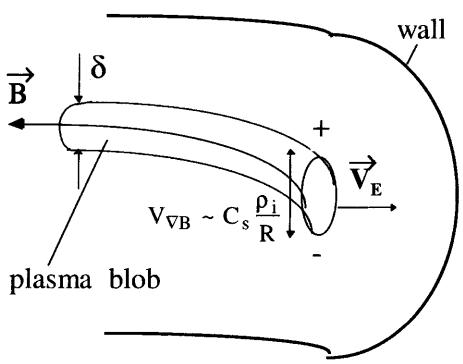

Fig. 3 ∇B plasma polarization and associated $\mathbf{E}\times\mathbf{B}$ drift result in outward motion of plasma blob in Tokamak far scrape off layer. (Ref. [16])

For simplicity, we assume that the SOL ion and electron temperature, T, is constant, and ignore the flow and the resistivity along the magnetic field lines. The electric current is described by

$$\nabla\cdot\mathbf{j}_\perp + \nabla\cdot\mathbf{j}_\parallel = 0, \tag{9}$$

where $\mathbf{j}_\perp = (\mathbf{B}\times\nabla P)/B^2$ and $\mathbf{j}_\parallel$ are the current densities perpendicular and parallel to the magnetic field line, respectively, $P = nT$ is the plasma pressure and n is the plasma density. In Eq. (9), $\nabla\cdot\mathbf{j}_\perp$ can be calculated as follows:

$$\begin{aligned}\nabla\cdot\mathbf{j}_\perp &= \nabla\cdot\left(\frac{\mathbf{B}\times\nabla P}{B^2}\right)\\ &= \nabla\left(\frac{1}{B^2}\right)\cdot(\mathbf{B}\times\nabla P) + \left(\frac{1}{B^2}\right)\mathbf{B}\cdot\cancel{(\nabla\times\nabla P)}\\ &\quad - \left(\frac{1}{B^2}\right)\nabla P\cdot(\nabla\times\mathbf{B}),\end{aligned} \tag{10}$$

where the second term becomes zero. We assume $\nabla P\cdot(\nabla\times\mathbf{B})\approx 0$, then the third term can be neglected. Hence,

$$\nabla\cdot\mathbf{j}_\perp = \nabla\cdot\left(\frac{\mathbf{B}\times\nabla P}{B^2}\right) \cong -\frac{T}{B^2}\nabla\ln B\cdot(\mathbf{B}\times\nabla n). \tag{11}$$

Integrating Eq. (9) along the magnetic field line gives

$$\int dl\,\frac{T}{B^2}\nabla\ln B\cdot(\mathbf{B}\times\nabla n) = \int dl\,\nabla\cdot\mathbf{j}_\parallel = 2j_\parallel|_{\text{target}}. \tag{12}$$

Here, $j_\parallel|_{\text{target}}$ is the current density at the end of the blob connected to the sheath. The coefficient of 2 means the blob is connect to the sheath at each end and we assume that the current density is equal at each end.

We can estimate $j_\parallel|_{\text{target}}$ by approximating the sheath resistivity R_{sheath} as

$$R_{\text{sheath}} = \frac{V_f}{I_{\text{sat}}} = \frac{\alpha T}{e n_T c_s}, \tag{13}$$

where V_f is the floating potential, I_{sat} is the ion saturation current in the sheath. n_T is the plasma density close to the wall, $c_s = \sqrt{T/m_i}$ is the ion acoustic speed, and $\alpha = (1/2)\ln[4\pi m_e/m_i] \approx 1$. Thus, $j_\parallel|_{\text{target}}$ accompanied with the electrostatic potential at the blob end ϕ which is caused by the ∇B drift is estimated as

$$j_\parallel|_{\text{target}} \approx e n_T c_s\left(\frac{e\phi}{T}\right). \tag{14}$$

From equation (12), we get

$$\frac{e\phi}{T} = \frac{\rho_i}{2n_T B}\int dl\,\nabla\ln B\cdot(\mathbf{B}\times\nabla n), \tag{15}$$

where $\rho_i = m_i v_\perp/(eB)$ is the ion sound Larmor radius and $v_\perp = \sqrt{T/m_i}$ is the ion thermal velocity. The magnetic curvature is evaluated by $\nabla\ln B = \hat{\mathbf{x}}/R$, where R is the major radius, x and y are the coordinates along radial and poloidal direction, respectively, and $\hat{\mathbf{x}}$ is the unit vector in the radial direction. We assume that the blob density is uniform along the magnetic field lines, and that the current density perpendicular to the field lines is uniform. Considering a plasma blob of density n_b with parallel length l_b, we obtain

$$\frac{e\phi}{T} = \frac{l_b\rho_i}{2Rn_T}\frac{\partial n_b}{\partial y}. \tag{16}$$

Approximating $\partial n_b/\partial y \approx n_b/\delta$, $E_y \approx \phi/\delta$, where δ is the poloidal scale length of the blob, then we get the rough estimation of the blob radial propagation velocity V_x as

$$V_x = c_s \left(\frac{\rho_i}{\delta}\right)^2 \frac{l_b}{R}\frac{n_b}{n_T}. \tag{17}$$

This equation indicates that a smaller blob has larger convective velocity. The stability of blobs should taken into account in blob transport since instability breaks blobs into pieces so that blob has a larger velocity than the original one. As a result, the first-wall might suffer from more radiation damages.

Even though the separable solution is just an example, it gives an estimate for the radial velocity of the blobs and provides an estimate of the radial distance, Δ_x, that the blob can travel during its life time, $\tau_b \approx l_b/c_s$, before terminating due to parallel plasma transport. Taking, as an estimate, $l_b \sim qR$, where q is the safety factor, from Eq. (17) we find

$$\Delta_x \approx V_x \tau_b \approx \left(\frac{\rho_i}{\delta}\right)^2 \frac{l_b^2}{R}\frac{n_b}{n_T}. \tag{18}$$

Analysis of the radial motion of isolated blobs makes sense only when $\Delta_x > \delta$, which gives

$$\delta < \delta_{max} = R\left\{\left(\frac{l_b \rho_i{}^2}{R^2}\right)\frac{n_b}{n_T}\right\}^{1/3}. \tag{19}$$

Using number of plasma particles in a blob $N_b \approx n_b l_b \delta^2$, another expression is obtained as

$$N_b \approx n_b l_b \delta^2 < n_b R^3 \left\{q^7 \left(\frac{\rho_i}{R}\right)^4\right\}^{1/3} \left(\frac{n_b}{n_T}\right)^{1/3}. \tag{20}$$

For a large Tokamak device, typical parameters are given by $q \sim 3$, $R \sim 1.5$m, $n_b \sim 10^{19}\mathrm{m}^{-3}$, $c_s \sim 3 \times 10^4$m/sec, $\rho_i/R \sim 2 \times 10^{-4}$, and $n_b/n_T \sim 10$. For the blob of the size $\delta \sim 0.01$m from eqs. (17)-(20), we find $V_x \sim 10^3$m/sec, $\Delta_x \sim 0.15$m, $\delta_{max} \sim 0.03$m, and $N_b \lesssim 10^{16}$ from equations (17)-(20).

2.3 Experimental Observation

In this section, experimental observation of plasma blob is shown. The evidence of plasma blob transport in the SOL is given in pictures taken by high-speed camera imaging. In recent years, high-speed cameras have become common and image quality is improved significantly. Currently, a rate of more than 10^5 frames per second is possible.

Fig. 4 shows an image taken at the spherical Tokamak NSTX with a high-speed camera. The images were produced by filtered D_α light with the use of a local gas puff in the camera field of view to increase the local neutral density and thus the brightness (and contrast) of the fluctuation images (Gas Puff Imaging Method). We can see the filament structure near the edge. This observation implies that the plasma blob structure is a type of filament along the magnetic field lines.

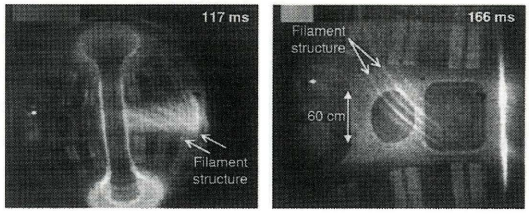

Fig. 4 Filament structure of plasma blob observed by gas puff imaging on NSTX. (Ref. [5])

Fig. 5 shows consecutive frames from an ultrafast camera of the D_α emission intensity fluctuation in a poloidal cross section in Alcator C-Mod Tokamak. Red and yellow colors correspond to positive fluctuation amplitudes, green and blue to negative. The separatrix position indicated as the black solid line. The picture shows the rapid convective propagation of the plasma blob in the SOL.

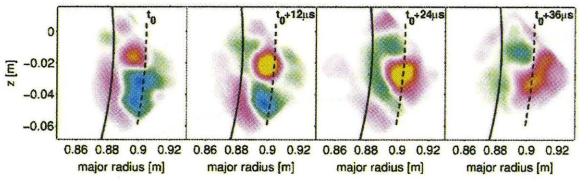

Fig. 5 The evolution of a long-living blob in Alcator C-Mod. (Ref. [6])

Fig. 6 shows the experimental results in DIII-D, visualized with the BES (Beam Emission Spectroscopy) diagnostics. We can find the density burst in plasma, and a structure, marked with a dotted circle and shown in both frames, undergoes both poloidal and radial motion, maintaining the clump structure.

3. Simulation of Blob Propagation

3.1 Model Equations

2D Hasegawa-Wakatani type model equations are introduced to describe the dynamics of blobs in SOL with local concentrations of density and vorticity. Derivation of the model equations is given in the paper D'Ippolito, *et al.*[17]. We follow the procedure to derive the model equations.

The model consists of the vorticity equation and the

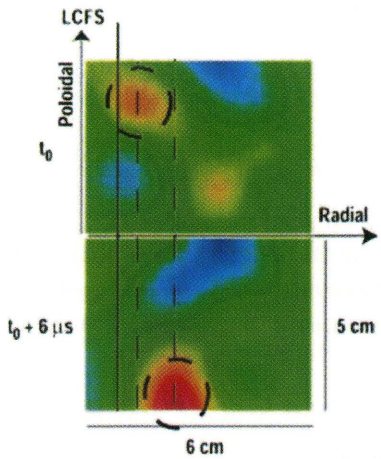

Fig. 6 Two frames from BES showing 2D density plots. Red indicates high density and blue low density. (Ref. [7])

continuity equation:

$$\frac{\mathrm{d}}{\mathrm{d}t}\nabla_\perp^2\Phi = \frac{B^2}{m_i n}\nabla_\parallel J_\parallel + \frac{2B}{m_i n}(\mathbf{b}\times\boldsymbol{\kappa})\cdot\nabla p \tag{21}$$

$$\frac{\partial n}{\partial t} + \nabla\cdot(n\mathbf{v}_e) = 0. \tag{22}$$

where $\mathrm{d}f/\mathrm{d}t = \partial f/\partial t + [\Phi, f]$, $[\Phi, f] = \mathbf{b}\cdot(\nabla_\perp\Phi\times\nabla_\perp f)$ is a Poisson bracket which indicates the convective derivative, $\mathbf{B} = B\mathbf{b}$ is the magnetic field, $\boldsymbol{\kappa} = \mathbf{b}\cdot\nabla\mathbf{b}$ is the magnetic curvature, $J_\parallel$ is the current density parallel to the ambient magnetic field, $\mathbf{v}_e$ is the electron flow velocity, $n = n_e = n_i$ is the particle density, $p = n(T_e + T_i)$ is the total pressure, and T_e and T_i are the electron and ion temperature. Here we assume $T_e \gg T_i$ and T_e is constant along the magnetic field lines. The Boussinesq approximation is used to derive the vorticity equation.

From Eq. (22), we obtain:

$$\left(\frac{\partial}{\partial t} + \mathbf{v}_e\cdot\nabla\right)n = -n\left(\nabla_\parallel v_{e\parallel} + \nabla_\perp\cdot\mathbf{v}_{e\perp}\right) \tag{23}$$

where, the perpendicular component of the electron drift velocity is given by

$$\mathbf{v}_{e\perp} = \frac{\mathbf{B}}{B^2}\times\mathbf{W}, \tag{24}$$

where

$$\mathbf{W} = \nabla\Phi - \frac{\nabla p}{ne} = \nabla\Phi - \frac{T_e}{e}\nabla\ln n. \tag{25}$$

The second term of R.H.S. of Eq. (23), is evaluated as

$$\begin{aligned}\nabla_\perp\cdot\mathbf{v}_{e\perp} &= -\frac{\nabla_\perp B^2\times\mathbf{B}}{B^4}\cdot\mathbf{W} \\ &\quad - \frac{\mathbf{B}}{B^2}\cdot\nabla_\perp\times\mathbf{W} + \frac{\mathbf{W}}{B^2}\cdot\nabla_\perp\times\mathbf{B} \\ &\simeq -\frac{\nabla B^2\times\mathbf{B}}{B^4}\cdot\mathbf{W},\end{aligned} \tag{26}$$

for the lowest order. Then Eq. (22) reduces to

$$\frac{\mathrm{d}n}{\mathrm{d}t} = -n\nabla_\parallel v_{e\parallel} + n\frac{2}{B}\boldsymbol{\kappa}\times\mathbf{b}\cdot\left(\nabla\Phi - \frac{T_e}{e}\nabla\ln n\right), \tag{27}$$

where the relation $\boldsymbol{\kappa} \simeq (\nabla_\perp B)/B$ is used.

Now, we calculate on the current density at the sheath. Electron flux is given by

$$\Gamma_e = n\int_{\sqrt{2e\Phi/m_e}}^{\infty}\mathrm{d}v_\parallel\, v_\parallel f(v_\parallel), \tag{28}$$

where we assume that $f(v_\parallel)$ is a Maxwellian distribution:

$$f(v_\parallel) = \left(\frac{m_e}{2\pi T_e}\right)^{3/2}\exp\left[\frac{-m_e v_\parallel^2}{2T_e}\right]. \tag{29}$$

Then the current density at the sheath is given by

$$J_{\parallel\mathrm{sh}} = en\left(c_s - \frac{v_{\mathrm{the}}}{\sqrt{2\pi}}\exp\left[-\frac{e\Phi}{T_e}\right]\right), \tag{30}$$

where $c_s = (T_e/m_i)^{1/2}$ is the ion acoustic speed and $v_{\mathrm{the}} = (T_e/m_e)^{1/2}$ is the electron thermal speed. Equations (21) and (27) can be simplified by integrating along the magnetic field lines from 0 to $L_\parallel$ in the limit where all quantities are assumed to be constant along the magnetic field line except the current, where $L_\parallel$ indicates the connection length of the magnetic field line in the SOL,

$$\begin{aligned}L_\parallel\frac{\mathrm{d}}{\mathrm{d}t}\nabla_\perp^2\Phi &= \frac{B^2}{m_i n}\left\{J_\parallel(L_\parallel) - J_\parallel(0)\right\} \\ &\quad + L_\parallel\frac{2B}{m_i n}(\mathbf{b}\times\boldsymbol{\kappa})\cdot\nabla p\end{aligned} \tag{31}$$

$$\begin{aligned}L_\parallel\frac{\mathrm{d}n}{\mathrm{d}t} &= -n\left\{v_{e\parallel}(L_\parallel) - v_{e\parallel}(0)\right\} \\ &\quad + L_\parallel n\frac{2}{B}\boldsymbol{\kappa}\times\mathbf{b}\cdot\left(\nabla\Phi - \frac{T_e}{e}\nabla\ln n\right).\end{aligned} \tag{32}$$

Assuming that both ends of each field line terminate at grounded conducting plates, and setting $J_\parallel(L_\parallel) = 2J_{\parallel\mathrm{sh}}$, $J_\parallel(0) = 0$ and $v_{e\parallel}(L_\parallel) = (v_{\mathrm{the}}/\sqrt{2\pi})\exp[-e\Phi/T_e]$, $v_{e\parallel}(0) = 0$, we get

$$\begin{aligned}\frac{\mathrm{d}}{\mathrm{d}t}\nabla_\perp^2\Phi &= \frac{1}{L_\parallel}\frac{2eB^2}{m_i}c_s\left(1 - \nu\exp\left[-\frac{e\Phi}{T_e}\right]\right) \\ &\quad + \frac{2B}{m_i n}(\mathbf{b}\times\boldsymbol{\kappa})\cdot\nabla p\end{aligned} \tag{33}$$

$$\begin{aligned}\frac{\mathrm{d}n}{\mathrm{d}t} &= -n\frac{1}{L_\parallel}c_s\nu\exp\left[-\frac{e\Phi}{T_e}\right] \\ &\quad + n\frac{2}{B}\boldsymbol{\kappa}\times\mathbf{b}\cdot\left(\nabla\Phi - \frac{T_e}{e}\nabla\ln n\right),\end{aligned} \tag{34}$$

where $\nu = (m_i/2\pi m_e)^{1/2}$. Introducing the normalization:

$$\begin{aligned}&\Omega_i t \to t, && \rho_s\nabla \to \nabla, && \rho_s\boldsymbol{\kappa} \to \boldsymbol{\kappa}, \\ &e\Phi/T_{es} \to \Phi, && n/n_s \to n, && T_e/T_{es} \to T, \\ &p/(n_s T_{es}) \to p,\end{aligned}$$

and using the relation

$$\Phi = \Phi_{\mathrm{B}} + \varphi,$$

where the Bohm potential is defined by $\Phi_{\mathrm{B}} \equiv T \ln \nu$, then we obtain

$$\frac{\mathrm{d}}{\mathrm{d}t}\nabla_\perp^2 \varphi = \alpha\sqrt{T}\left(1 - \exp\left[-\frac{\varphi}{T}\right]\right) + \frac{2}{n}\left(\mathbf{b}\times\boldsymbol{\kappa}\right)\cdot\boldsymbol{\nabla} p \tag{35}$$

$$\frac{\mathrm{d}n}{\mathrm{d}t} = -\alpha n \exp\left[-\frac{\varphi}{T}\right] + 2n\boldsymbol{\kappa}\times\mathbf{b}\cdot\left(\boldsymbol{\nabla}\varphi - \boldsymbol{\nabla}\ln n\right), \tag{36}$$

where the parameter $\alpha = 2\rho_{\mathrm{s}}/L_{\parallel}$ measures the net parallel current into the divertor plates.

Since the plasma filaments are assumed to be localized perpendicular to the magnetic field, we can use a slab model with orthogonal coordinates $\{x, y, z\}$ such that the x coordinate is taken in the direction of the major radius and the z coordinate is taken along the magnetic field line. The dimensionless curvature can be written as $\boldsymbol{\kappa} = -\left(\rho_{\mathrm{s}}/R\right)\hat{\mathbf{x}}$, where R is the major radius, $\hat{\mathbf{x}}$ is the unit vector in the x-direction, so that the second term of the R.H.S. of Eq. (35),

$$2\left(\mathbf{b}\times\boldsymbol{\kappa}\right)\cdot\boldsymbol{\nabla} = -\beta\frac{\partial}{\partial y}, \tag{37}$$

where $\beta = 2\rho_{\mathrm{s}}/R$ is the parameter measuring the strength of the curvature drift. Assuming $\varphi \ll 1$, and expanding exponential functions in (35) and (36), we obtain

$$\frac{\mathrm{d}}{\mathrm{d}t}\nabla_\perp^2\varphi = \alpha\varphi - \frac{\beta}{n}\frac{\partial n}{\partial y} + \mu\nabla_\perp^4\varphi \tag{38}$$

$$\frac{\mathrm{d}n}{\mathrm{d}t} = -\alpha n + \beta\left(n\frac{\partial\varphi}{\partial y} - \frac{\partial n}{\partial y}\right) + D\nabla_\perp^2 n, \tag{39}$$

where $\nabla_\perp^2 = \partial^2/\partial x^2 + \partial^2/\partial y^2$ and the ion viscosity μ and the diffusion coefficient D are introduced. These equations are full nonlinear model equations used in Section 3.2 and later in Chapter 4. Further simplification is possible, if we assume that the density modulation is weak, we linearize the second term in R.H.S. of Eq. (38) and the second term in R.H.S. of Eq. (39), then we have partially linearized model equations

$$\frac{\mathrm{d}}{\mathrm{d}t}\nabla_\perp^2\varphi = \alpha\varphi - \beta\frac{\partial n}{\partial y} + \mu\nabla_\perp^4\varphi \tag{40}$$

$$\frac{\mathrm{d}n}{\mathrm{d}t} = -\alpha n + \beta\left(\frac{\partial\varphi}{\partial y} - \frac{\partial n}{\partial y}\right) + D\nabla_\perp^2 n. \tag{41}$$

The energy conservation relation in this system is written as,

$$\begin{aligned}\frac{\mathrm{d}}{\mathrm{d}t}\langle H\rangle = &-\alpha\left\langle\left(|\varphi|^2 + |n|^2\right)\right\rangle \\ &-\mu\left\langle\left|\nabla_\perp^2\varphi\right|^2\right\rangle - D\left\langle\left|\nabla_\perp^2 n\right|^2\right\rangle,\end{aligned} \tag{42}$$

where, the bracket $\langle\rangle$ is the surface integral given by

$$\langle\rangle \equiv \frac{1}{L_x L_y}\int_0^{L_y}\int_0^{L_x}\mathrm{d}x\,\mathrm{d}y,$$

and

$$H = \frac{1}{2}\left(\left|\nabla_\perp^2\varphi\right|^2 + |n|^2\right)$$

is the Hamiltonian of this system.

If we ignore the second term in R.H.S. of Eq. (39), these equations reduce to the model used for calculating the blob dynamics during transport in the SOL in Ref. [8].

3.2 Numerical Scheme and Boundary Conditions

We have developed the spectral and pseudo-spectral codes to solve Equations (38)-(41). Pseudo-spectral methods are introduced to solve the full nonlinear model equations ((38) and (39)) in the following sections. The nonlinear term associated with the density in the model equations, i.e. the second term of the R.H.S. of Eq. (38) is difficult to describe in Fourier-space. The pseudo-spectral method has an advantage to calculate such nonlinear terms.

In the spectral code, the equations are solved numerically by the finite difference in the x-direction, and by the Fourier expansion in y-direction The nonlinear terms are evaluated in Fourier space. In the pseudo-spectral code, the nonlinear terms are evaluated in the real space using Fast Fourier Transform (FFT).

The following boundary conditions are used for the blob transport. In the vorticity equation,

$$\begin{aligned}&\text{for } m = 0: \quad \nabla_\perp^2\varphi'(x=0) = 0, \quad \nabla_\perp^2\varphi(x=L_x) = 0\\ &\text{for } m \neq 0: \quad \nabla_\perp^2\varphi(x=0) = 0, \quad \nabla_\perp^2\varphi(x=L_x) = 0\end{aligned}$$

where the prime means the derivative of x, and L_x indicates the system size of the x direction. Similarly,

$$\begin{aligned}&\text{for } m = 0: \quad \varphi'(x=0) = 0, \quad \varphi(x=L_x) = 0\\ &\text{for } m \neq 0: \quad \varphi(x=0) = 0, \quad \varphi(x=L_x) = 0\end{aligned}$$

are imposed. In the continuity equation,

$$\begin{aligned}&\text{for } m = 0: \quad n(x=0) = n_0, \quad n'(x=L_x) = 0\\ &\text{for } m \neq 0: \quad n(x=0) = 0, \quad n'(x=L_x) = 0\end{aligned}$$

are imposed.

The periodic boundary condition is used in the y-direction such as $\varphi(y=0) = \varphi(y=L_y)$, where L_y is the system size of the y direction.

The initial blob density distribution is given by Gaussian:

$$\text{Blob Density Distribution}\,(x,y) = n_{\mathrm{b}}\exp\left[-\left(\frac{x-2\delta_{\mathrm{b}}}{\delta_{\mathrm{b}}}\right)^2 - \left(\frac{y-L_y/2}{\delta_{\mathrm{b}}}\right)^2\right]$$

where δ_b represents the blob radius. For simulation parameters, we choose $n_b/n_0 = 10$, $\mu = D = 2 \times 10^{-3}$, 256 radial grids, and 128 Fourier modes for spectral code and 256 Fourier modes for the pseudo-spectral codes.

3.3 Partially Linearized Model

In this section, we show the simulation results solving the equations (40) and (41), in which the density nonlinear terms are linearized . The partially linearized model equations can be solved by both spectral and pseudo-spectral methods. The pseudo-spectral code is compared with the spectral code for code validation, then we use the pseudo-spectral code for simulations demonstrated in the after sections.

3.3.1 Comparison between Spectral and Pseudo-Spectral Codes

In this subsection, we compare the simulation results of the power spectra by spectral and pseudo-spectral codes.

Figures 3.1 shows the power spectra of electrostatic potential and density in the small blob simulations ($\delta_b = 5$). In the early phase of the nonlinear evolution, the power spectra coincide with each other. As time goes by, the difference between the spectral method and the pseudo-spectral method is observable. However, the difference is negligible in low mode region, so that we may consider both codes correctly work.

Fig. 3.2 shows the time evolution of the density energy for the largest 10 Fourier modes. Although the similar behavior is observed for the spectral and the pseudo-spectral code for $t < 1000$, the dissipation in the pseudo-spectral code results are somewhat stronger than that in the spectral code. For $t > 1000$, the complicated behavior of high modes is observed in the pseudo-spectral code, which is different from those in the spectral code. This behavior might be related with the chaotic nature of the system. Since the dealiasing is not applied in this version of the pseudo-spectral code, there exists noise in the high k_y region, which might lead to different behavior of high k_y modes due to the sensitivity of a initial value.

Figures 3.3 shows the power spectra in the large blob simulations ($\delta_b = 60$). In this case, the agreement between two codes is fairly well compared to the case with the small blob. However, we can see the accumulation of energies in the high-mode region as time goes by, in the pseudo-spectral case. Some care should be taken into account to get rid of the aliasing error in the pseudo-spectral code for long time simulations.

3.3.2 Small Blobs

In the previous section, we validate the spectral and the pseudo-spectral codes. In this subsection, we focus on our simulation results of the blob propagation in the SOL using the pseudo-spectral code. The blob instabilities that occur during propagation in the SOL and affected by the blob size are investigated by Aydemir [8]. The characteristic blob size a_m is introduced, which

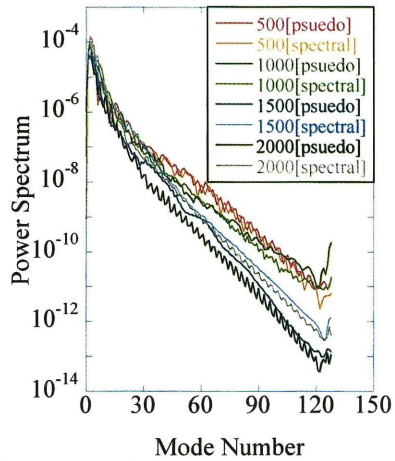

(a) Power spectra of the electrostatic potential in the small blob propagation simulations solved by the spectral and the pseudo-spectral codes.

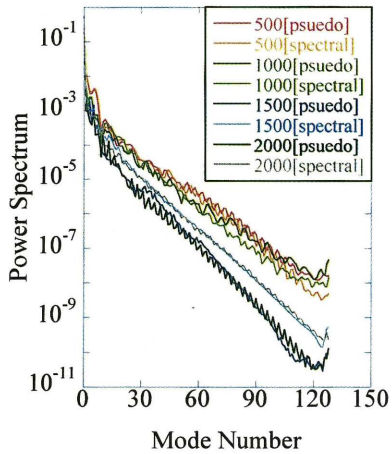

(b) Power spectra of the plasma density in the small blob propagation simulations solved by the spectral and the pseudo-spectral codes.

Fig. 7 Line colors refer to the time step of the simulation results by the spectral and the pseudo-spectral codes. Vertical axis indicates the energy of the power spectra and horizontal axis indicates the Fourier mode number in the poloidal direction.

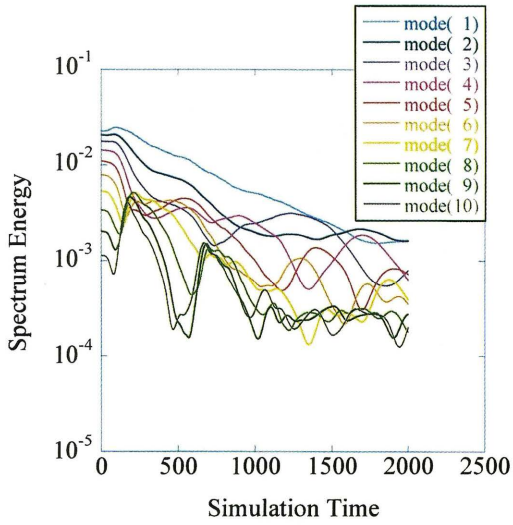

(a) Spectral code is used in this simulation.

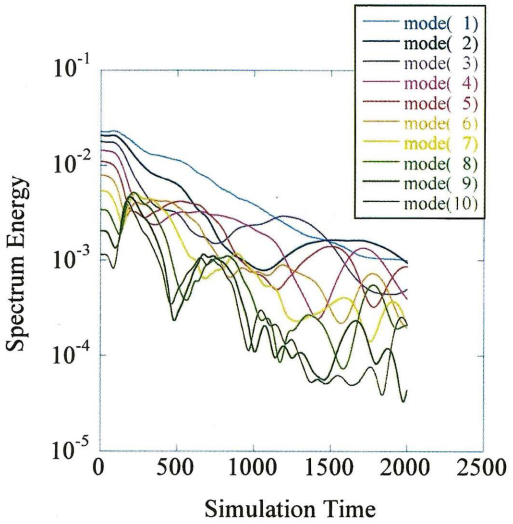

(b) Pseudo-spectral code is used in this simulation.

Fig. 8 Time evolution of the spectrum energies of the plasma density in the small blob ($\delta_b = 5$) propagation simulations. Line colors refer to the spectral and the pseudo-spectral mode numbers.

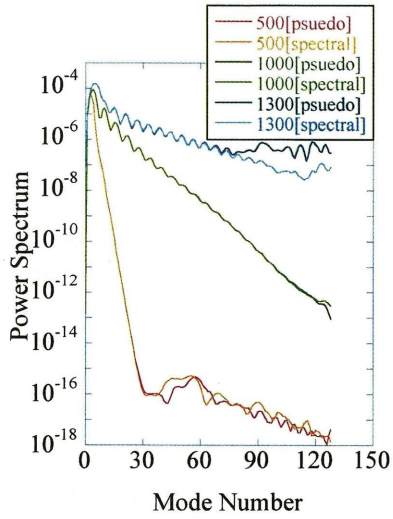

(a) Power spectra of the electrostatic potential in the large blob propagation simulations solved by the spectral and the pseudo-spectral codes.

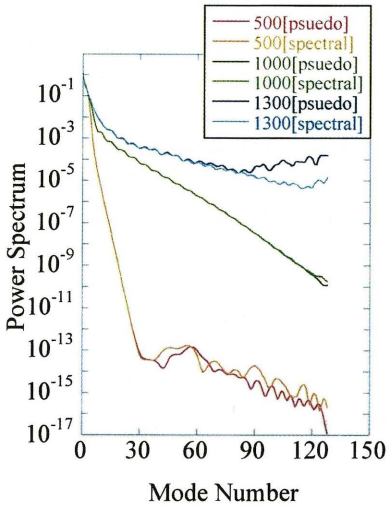

(b) Power spectra of the plasma density in the large blob propagation simulations solved by the spectral and the pseudo-spectral codes.

Fig. 9 Line colors refer to the time step of the simulation results by the spectral and the pseudo-spectral codes. Vertical axis indicates the energy of the power spectra and horizontal axis indicates the Fourier mode number in the poloidal direction.

gives the categorization of the type of blob instabilities

$$a_m = \rho_s \left(\frac{L^2}{2\rho_s R} \right)^{1/5}, \tag{43}$$

where R is the major radius, $L = qR$ is the connection length of the magnetic field line in the SOL.

Using large Tokamak parameters: $c_s = 6 \times 10^4$m/sec, $\Omega_i = 10^8 \mathrm{sec}^{-1}$, $L = 40$m, and $R = 2$m (similar to the parameters used by Yu and Krasheninnikov [11]), we get $\alpha = 3 \times 10^{-5}$, and $\beta = 6 \times 10^{-4}$. These gives the dimensionless length scale $a_m = 15$ (in units of $\rho_s = 6 \times 10^{-4}$m). We simulate the process of nonlinear evolution in blob propagation with respecting to a_m.

First, we show the result of small blob propagation in Fig. 10. Here, we take the blob size as $\delta_b = 5$ ($\delta_b/a_m <$

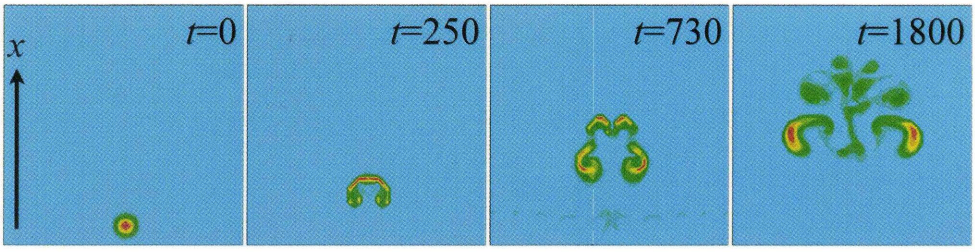

Fig. 10 Nonlinear evolution of the small blob (δ_b=5) with the partially linearized model. In this and following figures, the bottom boundary represents the separatrix (or the last closed flux surface). The horizontal and vertical coordinates are the poloidal and radial directions, respectively. The red and yellow colors correspond to high density, blue and green to low. The field size of this result is 128 in x and is 128 in y. The lengths are in units of $\rho_s = 6 \times 10^{-4}$m. Time is normalized to $\Omega_i^{-1} = 1 \times 10^{-8}$sec.

1). The rapid convection occurs and the velocity shear is generated, which gives rise to the formation of Kelvin-Helmholtz vortices and vortex shedding. As a result, small blobs do not survive as coherent structures.

Fig. 11 shows the radial density profile of $m = 0$ mode in the early stage of nonlinear evolution. In this stage, the blob remains as a coherent structure. The initial Gaussian profile advects radially as a pulse with a front and tail. The peak of the Gaussian profile convects rapidly due to the formation of large electrostatic potential which gives rise to the large $\mathbf{E} \times \mathbf{B}$ drift velocity. Accompanied with its effect, the shape of the density profile gets gradually steepening. The radial profile of the propagating blob resembles "shock-wave" solutions of the Burgers' equation, as mentioned in earlier works [8), 13)].

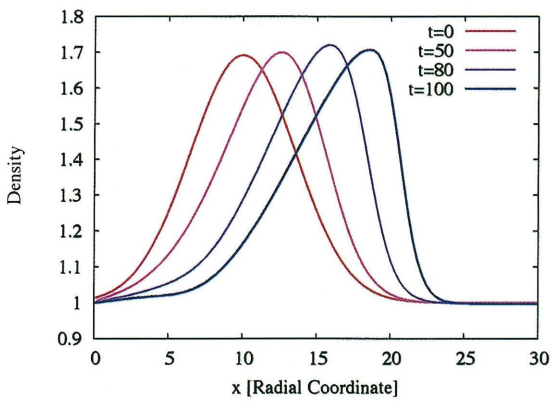

Fig. 11 Radial density profile of $m = 0$ mode in the small blob ($\delta_b = 5$) propagation using the partially linearized model equations. In this stage of evolution, the blob form remains the coherent structure.

3.3.3 Large Blobs

Large blobs are not affected by Kelvin-Helmholtz instabilities since their convective velocities are small. Fig. 12 shows the simulation results, with $\delta_b = 60$ ($\delta_b/a_m \gg 1$). It is seen that "Rayleigh-Taylor fingers" develop. In this case, interchange instabilities play a dominant role in the large blob propagation. We also find that rapid dissipation occurs.

During the evolution of large blobs, their initial structure survives longer than that of small blobs. The peak value decreases according to the deformation of blob due to interchange instability. The steepening effect is observed here, also.

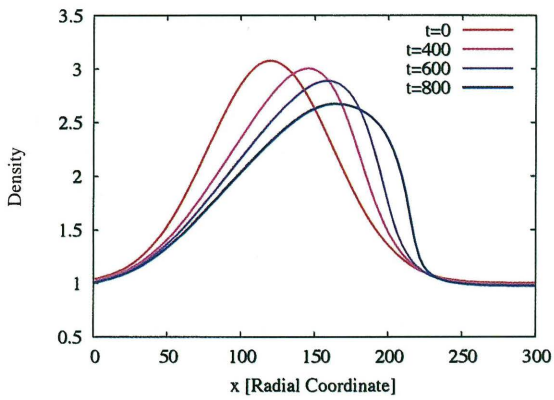

Fig. 13 Radial density profile of $m = 0$ mode in the large blob ($\delta_b = 60$) propagation using the partially linearized model equations. In this stage of evolution, the blob form remains the coherent structure.

3.4 Full Nonlinear Model

In this section, we investigate the effect of density nonlinearity in Equations (38) and (39). Such nonlinearity

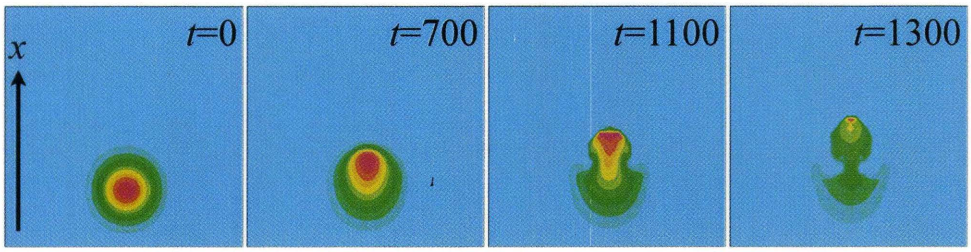

Fig. 12 Nonlinear evolution of the large blob of size $\delta_b = 60$ with the partially linearized model. The other parameters are same as in Fig. 10. The field size is 512 in each direction.

can be treated by the pseudo-spectral method. We compare the results with those in the previous section and clarify the effect of density nonlinearity. Simulation results are discussed in detail in the following subsections.

3.4.1 Small Blobs

The Kelvin-Helmholtz vortices and the instabilities are observed in Fig. 14, similar to the previous section. However, the time scale of propagation is quite slow in the case of density nonlinearity. For example, the blob structure at $t = 600$ in Fig. 14 is similar to the one at $t = 200$ in Fig. 10, which implies the density nonlinearity has a tendency to slow down the evolution of Kelvin-Helmholtz instability. The vortex breaks up into pieces at $t = 1100$. In Fig. 10, break up vortices are dragged by the front head of vortex and form a complicated convective structure. On the other hand, the vortices break up and dissipate in Fig. 14.

Fig. 15 is the radial density profile of $m = 0$ mode in this simulation. This figure indicates the effect of density nonlinearity that makes the blob propagation velocity slow. For example, the x coordinate of the peak in the radial density profile at $t = 80$ in Fig. 15 is clearly larger than that in Fig. 11. We can see that the steepening effect is weaker in this full nonlinear case. For example, the heads and tails of the blob radial profile at $t = 100$ in Fig. 11 and at $t = 160$ in Fig. 15 bear a strong resemblance to each other, however the peak of the profile in Fig. 15 clearly decays. In fact, after the last time step drawn in Figures 11 and 15, they lose their coherent structure because of Kelvin-Helmholtz instabilities.

We focus on the blob propagation velocities here. In Fig. 16, the point sets show the time series over the range t = 0-100 in the partially linearized model and t = 0-160 in the full nonlinear model of small blob propagation. In these ranges, the blob remains the coherent structure. Because of the limitation of the grid number in x direction, the point sets are not smooth. We introduce a quadratic function to fit these data sets with the least-square method. The used equations and parameters are follows:

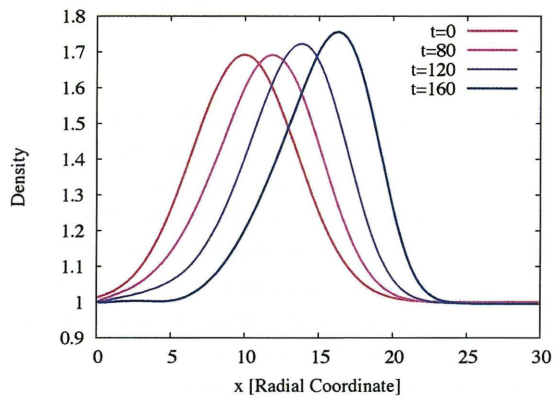

Fig. 15 Radial density profile of $m = 0$ mode in the small blob ($\delta_b = 5$) propagation using the full nonlinear model in the early stage of nonlinear evolution. At this stage, the blob remains a coherent structure.

$$
\begin{aligned}
f(t) = {} & \left(6.43168 \times 10^{-4} \pm 1.019 \times 10^{-5}\right) t^2 \\
& + \left(2.33722 \times 10^{-2} \pm 1.053 \times 10^{-3}\right) t \\
& + \left(9.80925 \pm 2.278 \times 10^{-2}\right) \\
g(t) = {} & \left(1.98346 \times 10^{-4} \pm 3.149 \times 10^{-6}\right) t^2 \\
& + \left(9.32051 \times 10^{-3} \pm 5.208 \times 10^{-4}\right) t \\
& + \left(9.88098 \pm 1.803 \times 10^{-2}\right)
\end{aligned}
$$

where $\pm$ indicates the error, $f(t)$ fit the partially linearized model data set, and $g(t)$ fit the full nonlinear model data set. The velocity is given by time derivative of $f(t)$ and $g(t)$. We obtain the small blobs propagation velocities which relax to constant after enough time passed. For the model without density nonlinearity $\dot{f}(80) \sim 1.26 \times 10^{-1}$ and for the model with density nonlinearity $\dot{g}(140) \sim 6.49 \times 10^{-2}$, where ' $\cdot$ ' means time derivative, which indicates the propagation velocity with density nonlinearity is about 3 times slower than that without the density nonlinearity in the case of the small blobs. These estimations are used in next

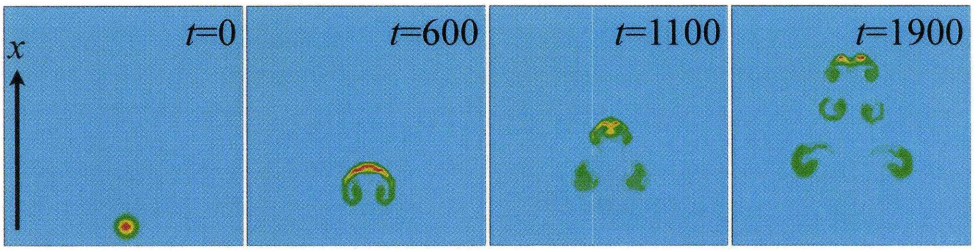

Fig. 14 Nonlinear evolution of small blob ($\delta_b = 5$, $\delta_b/a_m < 1$) with full nonlinear model equations. Other parameters are the same as in Fig. 10. The system size is 128 in each direction.

subsection to compare the large and small blobs propagation velocities based on the estimation equation (17).

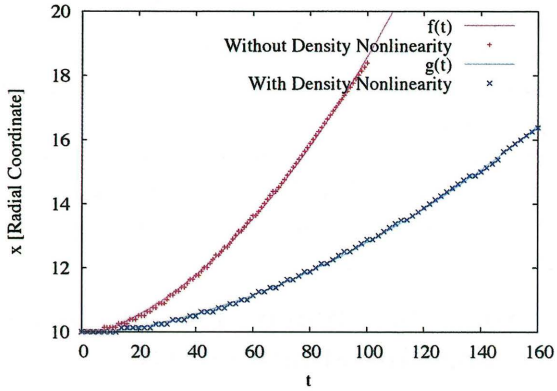

Fig. 16 The peak locations of $m = 0$ mode for the density versus time, fitted with the quadratic functions using the least-square method.

3.4.2 Large Blobs

Fig. 17 shows nonlinear evolution of the large blob in the case with density nonlinearity. The propagation velocity is slow enough to develop the Rayleigh-Taylor fingers in this case.

The steepening effect weakly appears in this case also, especially compare to Fig. 13. It should be noted that the propagation velocity is quite slow. The blob remains the coherent structure of itself in the time stage captured in this Fig. 18, and after the last time step, they lose their coherent structure because of interchange instability.

Here, we have the same propagation velocity estimation as in previous subsection. In Fig. 19, the point set show the time series over the range t = 0-600 in the partially linearized model and t = 0-3000 in the full nonlinear model of large blob propagation. In these ranges, the blob remains the coherent structure. The

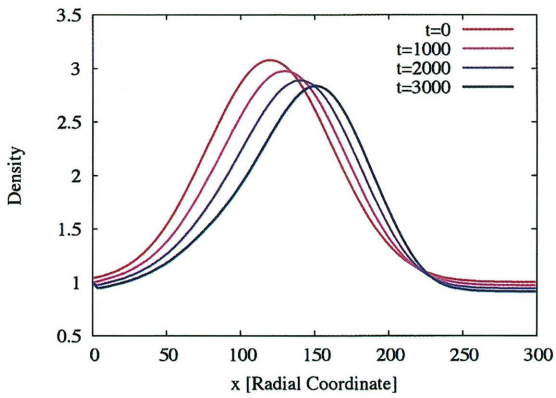

Fig. 18 Radial density profile of $m = 0$ mode in the large blob ($\delta_b = 60$) propagation using the full nonlinear model in the early stage of nonlinear evolution. At this stage, the blob remains a coherent structure.

used quadratic function and the parameters to fit the data sets in the least-square method are follows:

$$\begin{aligned} h(t) &= \left(7.50336 \times 10^{-6} \pm 2.048 \times 10^{-6}\right) t^2 \\ &\quad + \left(6.37899 \times 10^{-2} \pm 1.27 \times 10^{-3}\right) t \\ &\quad + \left(118.365 \pm 0.1648\right) \\ k(t) &= \left(2.28985 \times 10^{-7} \pm 2.041 \times 10^{-8}\right) t^2 \\ &\quad + \left(9.65625 \times 10^{-3} \pm 6.329 \times 10^{-5}\right) t \\ &\quad + \left(120.077 \pm 4.107 \times 10^{-2}\right) \end{aligned}$$

where $\pm$ indicates the error, $h(t)$ fit the partially linearized model data set, and $k(t)$ fit the full nonlinear model data set. The velocity is given by time derivative of $h(t)$ and $k(t)$.

Here, we obtain the large blob propagation velocity at the same t discussed at the end of the previous subsection. For the model without density nonlinearity $\dot{h}(80) \sim 6.5 \times 10^{-2}$ and for the model with density nonlinearity $\dot{k}(140) \sim 9.72 \times 10^{-3}$ which indicates that the propagation velocity with the density nonlinearity is about 6.5 times slower than that without the den-

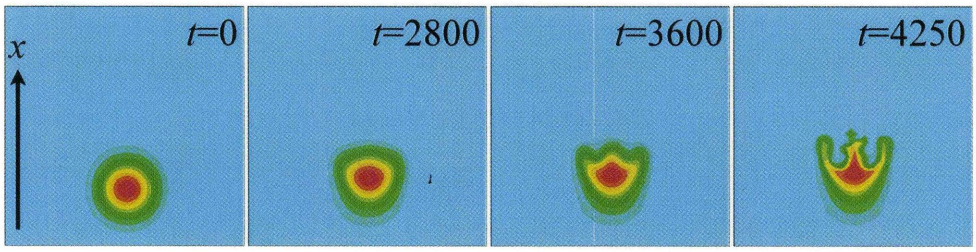

Fig. 17 Nonlinear evolution of the large blob ($\delta_b = 5$, $\delta_b/a_m \gg 1$) with the full nonlinear model. Other parameters are same as in Fig. 10. The system size is 512 in each direction.

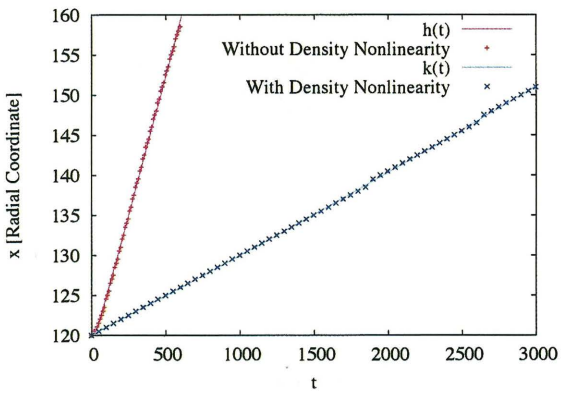

Fig. 19 The peak location of $m = 0$ mode for the density versus time, fitted with the quadratic functions using the least-square method.

sity nonlinearity in the case of large blobs. Now we consider the blob propagation velocity estimation equation (17), it indicates that the propagation velocity is inverse proportion to square of blob size. In this work, we use $\delta_{b\,\mathrm{small}} = 5$ and $\delta_{b\,\mathrm{large}} = 60$, thus the velocity ratio must be $V_{x\,\mathrm{large}}/V_{x\,\mathrm{small}} \sim 12^2$. Here the velocity ratio of models without density nonlinearity is $\dot{h}(80)/\dot{f}(80) \sim 1.9$ and the ratio of models with density nonliearity is $\dot{k}(140)/\dot{g}(140) \sim 13$. Both of them are far from linear estimation of Eq. (17). It is probably because of the derivation of Eq. (17) is based on the assumption that the solution has the form of a traveling wave and it is even in y. However, these assumption must not be valid in general and the solution for the potential does not satisfy any reasonable boundary conditions. Therefore, we should regard this estimation just gives the qualitative tendency of simulation results.

3.5 Effect of Density Nonlinearity

In the previous section, we discussed on the effects of the density nonlinearities. However it is not revealed that which density nonlinearity is effective, $n^{-1}\,\partial n/\partial y$ in Eq. (38) or $n\,\partial\varphi/\partial y$ in Eq. (39). We show the comparison of the power spectra with the full nonlinear model ((38) and (39)) and with the semi-nonlinear model in which $n\,\partial\varphi/\partial y$ term is replaced by $\partial\varphi/\partial y$ in the continuity equation. Figures 3.14 and 3.15 show the power spectra obtained by the small and the large blob propagation simulations with full nonlinear model and semi-nonlinear model.

The good agreement of the power spectra in each time step is observed, which indicates the dominant contribution of the density nonlinearity is $n^{-1}\,\partial n/\partial y$ in the vorticity equation.

4. Nonlinear Simulation of Interchange Instability in SOL

4.1 Linear Analysis

In the previous chapter, we have shown that the interchange modes are responsible for the large blob dynamics during propagation in the SOL with simulations in which, we assume the blob structure as the initial condition. The interchange mode also plays an important role in the stability of the background SOL plasma. In this chapter, we investigate the SOL interchange turbulence, which creates blobs near the separatrix, and the SOL density profile, which produced by the consistent simulation from blob creation at the separatrix to blob propagation in the SOL.

Firstly, the linear growth rate of the SOL interchange instability is evaluated by linearizing Equations (40) and (41). The local dispersion relation is given by

$$\left(i\omega k_\perp^2 - \alpha - \mu k_\perp^4\right)\left(-i\omega + \alpha + ik_y\beta + Dk_\perp^2\right) + ik_y\beta\left(-\frac{ik_y}{\lambda} + ik_y\beta\right) = 0, \tag{44}$$

where $k_\perp^2 = k_x^2 + k_y^2$, k_x and k_y are the wave numbers in the radial and poloidal directions, respectively. The equilibrium density is modeled by $n_0 = \tilde{n}_0 \exp\left[-x/\lambda\right]$. Solving this equation for ω and taking the imaginary part, the growth rate γ of the interchange modes in the SOL plasmas is obtained. When dissipation is included,

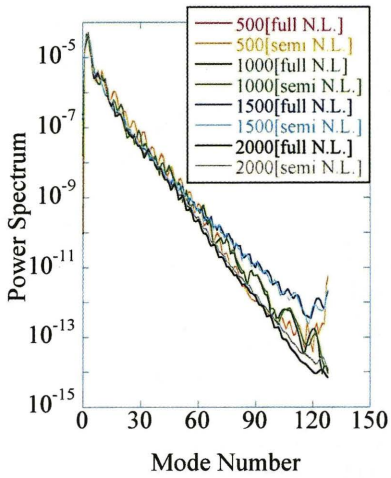

(a) Power spectra of the electrostatic potential by the small blob propagation simulations with the full nonlinear model and the semi-nonlinear model.

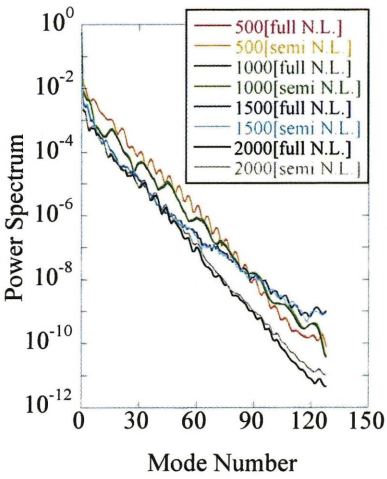

(b) Power spectra of the density by the small blob propagation simulations with the full nonlinear model and the semi-nonlinear model.

Fig. 20 Line colors refer to the time step of the full nonlinear model and the semi-nonlinear model. Vertical axis indicates the strength of the power spectrum and horizontal axis indicates the Fourier mode number in the poloidal direction.

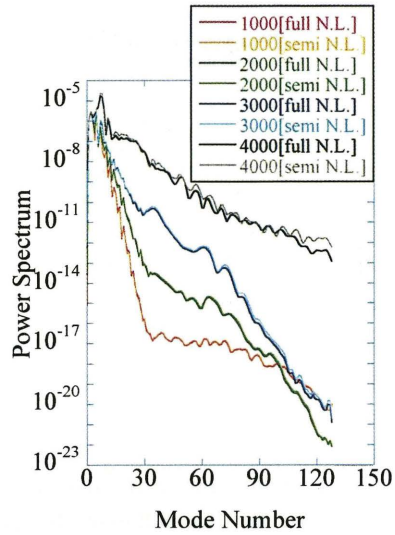

(a) Power spectra of the electrostatic potential by the large blob propagation simulations with full nonlinear model and semi-nonlinear model.

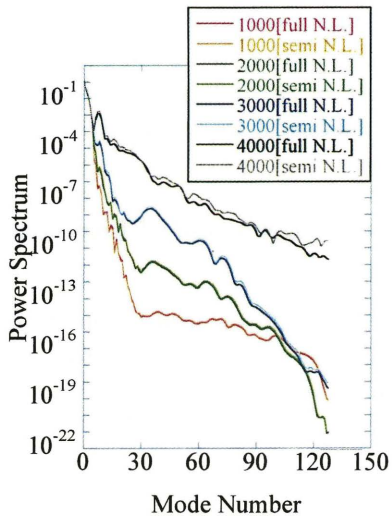

(b) Power spectra of the plasma density by the large blob propagation simulations with full nonlinear model and semi-nonlinear model.

Fig. 21 Line colors refer to the time step of the full nonlinear model and the semi-nonlinear model. Vertical axis indicates the strength of the power spectrum and horizontal axis indicates the Fourier mode number in the poloidal direction.

there is a $k_{\max}$ such that modes with $k_y > k_{\max}$ are stable. However, this cutoff in k_y requires both coefficients μ and D to be finite. Fig. 22 shows the dependence of the growth rate on the poloidal wave number k_y. Two cases with different dissipation rates are investigated. It is shown that the strong dissipation suppresses the growth of interchange instabilities.

Figures 4.2 show the dependence of the growth rate on k_y for different values of α (fig. 4.2(a)) and β (fig. 4.2(b)) in the case with $\mu = D = 2 \times 10^{-2}$. Fig. 4.2(a) shows that α does not contribute to the cutoff wave number $k_{\max}$ above which the mode is stable. However,

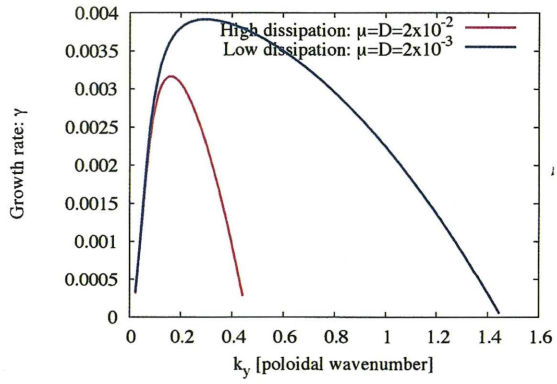

Fig. 22 Growth rate of the SOL interchange modes as a function of the poloidal wave number k_y for two different dissipation rates, with $\alpha = 3 \times 10^{-5}$, $\beta = 6 \times 10^{-4}$, and $\lambda = 32$.

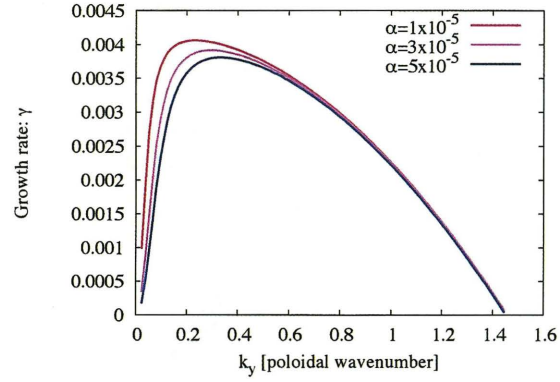

(a) k_y dependency of the linear growth rate as the scale length on the influx current into the divertor plate α is varied with $\beta = 6 \times 10^{-4}$ and $\lambda = 32$.

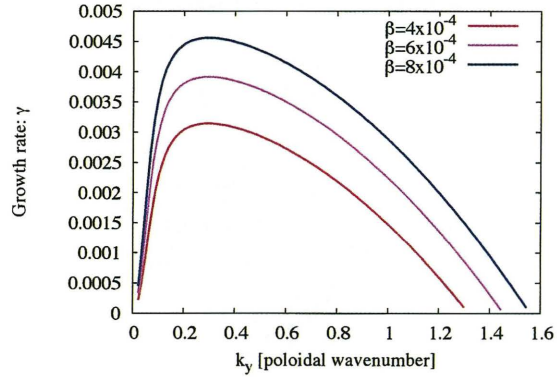

(b) k_y dependency of the linear growth rate as the scale length of the strength of the curvature drift β is varied with $\alpha = 3 \times 10^{-5}$ and $\lambda = 32$.

Fig. 23 Plot of the growth rate of the SOL interchange modes with $\mu = D = 2 \times 10^{-2}$.

the wave number at the maximum of the growth rate shift to the long wave length side when α decreases. On the other hand, in fig. 4.2(b), β does not contribute to the wave number at the maximum, however $k_{\max}$ increases with β.

4.2 Nonlinear Evolution of Interchange Instability

The simulation conditions used in this chapter is almost the same as in the previous chapter. The differences are follows. In the continuity equation, the boundary conditions are given by

$$\text{for } m = 0 \text{ mode:} \quad n'(x=0) = 0, n(x = L_x) = 0$$
$$\text{for } m \neq 0 \text{ mode:} \quad n(x=0) = 0,\ n(x = L_x) = 0.$$

The initial density profile is given as exponential, the half maximum of full width is given by $\lambda = 30$. Other parameters are assumed as follows: $\alpha = 3 \times 10^{-5}$, $\beta = 6 \times 10^{-4}$, $\mu = D = 2 \times 10^{-3}$, 512 radial grids, 512 Fourier modes.

The initial perturbation is given by a blob like one with the size of 30. In the early stage of time evolution, the localized perturbation of the electrostatic potential extends over the poloidal direction, and the wave like structure (see Fig. 24) forms. The density fluctuations increase (at $t = 4500$) and the "Rayleigh-Taylor fingers" develop (at $t = 5040$). In the detach event (at $t = 5800$), the velocity shear accompanied with the gradient of the electric field plays an important role.

4.3 Simulation with Density Source

In this section, we introduce the density source term into the continuity equation:

$$\frac{\mathrm{d}}{\mathrm{d}t}\nabla_\perp^2\varphi = \alpha\varphi - \frac{\beta}{n}\frac{\partial n}{\partial y} + \mu\nabla_\perp^4\varphi \tag{45}$$

$$\frac{\mathrm{d}n}{\mathrm{d}t} = -\alpha n + \beta\left(n\frac{\partial\varphi}{\partial y} - \frac{\partial n}{\partial y}\right) + D\nabla_\perp^2 n + S(x). \tag{46}$$

The source term is given as exponential, the half maximum of full width is given by $\lambda = 8$. The origin of the source term comes from the particle flux from core plasma across the separatrix. The other simulation conditions are almost the same as in the section 4.2.

Fig. 25 shows the time evolution of SOL interchange turbulence with density source. The structure is clearly different from Fig. 24. In the simulation with source, the density profile evolves gradually, and many modes

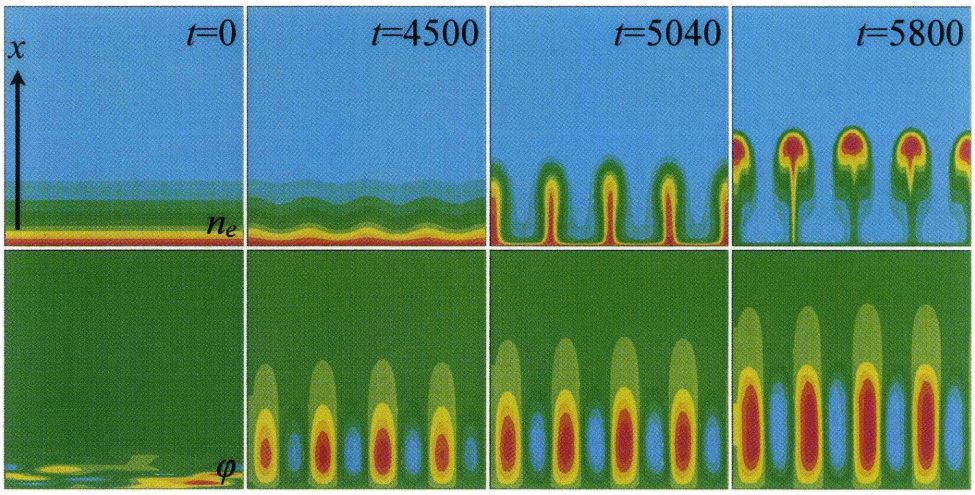

Fig. 24 Nonlinear evolution of the interchange instability at the separatrix with blob like perturbation. Pictures above demonstrate the plasma density and below demonstrate the electrostatic potential distribution at the same time step. The vertical axis indicates the radial direction and the horizontal axis indicates the poloidal direction. The bottom of each plot assumed as the separatrix. The time step is normalized to $\Omega_i^{-1} = 1 \times 10^{-8}$sec. The simulation field size is 256×256, normalized to $\rho_s - 6 \times 10^{-4}$m.

are destabilized simultaneously. Thus, Fig. 25 shows more complicated structure than Fig. 24 where single mode is destabilized.

It is seen that the "Rayleigh-Taylor fingers" develop at $t = 1680$, detachment events occur at $t = 1880$ and turbulence develop at $t = 2300$. We can see a lot of dipole structures of electrostatic potential in each stage. These vortex move out according to the $\mathbf{E} \times \mathbf{B}$ drift after $t = 2300$, the density structure becomes more complicated and the density fluctuation extends to the x direction.

Fig. 26 shows the radial density profile of $m = 0$ mode at each time step in Fig. 25. The density increases from $t = 1000$ to $t = 1680$, then it abruptly decrease due to blob detachment at $t = 1880$ and gradually extend to the radial direction after that.

This intermittent and convective structure of plasma transport in the SOL region could be estimated quantitatively using the statistical analysis. It is left for a future work.

Fig. 27 shows the radial density profile of the $m = 0$ mode at $t = 4000$ and the exponential density fitting curve with the least-square method. Here, we demonstrate the good fit by exponential function which structure indicates the normal diffusion profile. The energy of the other modes are smaller than $m = 0$ which is about the order of $O(10^{-2})$, and they contribute the intermittent density structure. This result shows that 2nd SOL is not reproduced in this simulation.

For the future work, we should couple with plasma core and SOL to incorporate more realistic source term

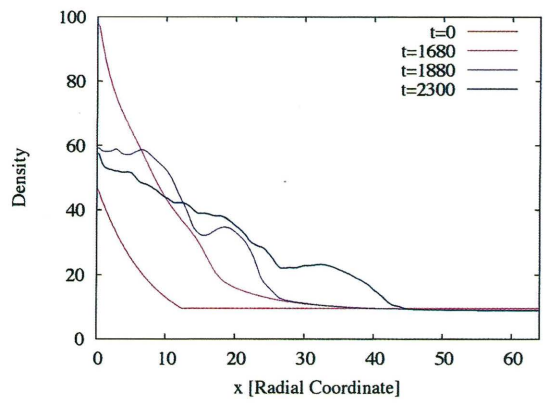

Fig. 26 Radial density profiles of $m = 0$ mode at each time step in Fig. 25. x range is restricted to half of simulation field.

into the model and investigate parameter region where the convection is dominant compared to the diffusion process.

5. Summary and Discussion

The radial convective propagation and the formation of the plasma blob structure in the SOL region has been investigated by using 2D Hasegawa-Wakatani type equations. We summarize our work here.

1. The spectral and the pseudo-spectral codes are developed for the partially linearized model and are compared each other for code validation, then the pseudo-spectral code is used for simulation study.

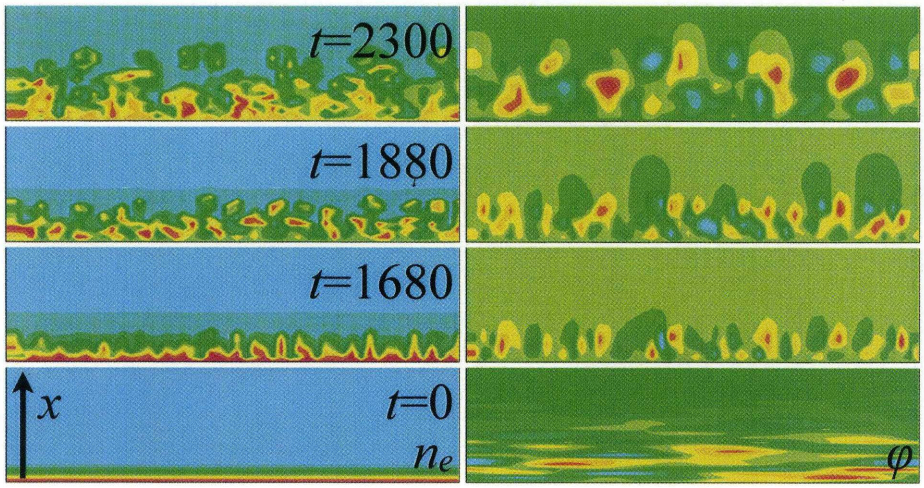

Fig. 25 The time evolution of SOL interchange instability with density source. The left side four plots show the density and the right side four show the electrostatic potential. t is the time step scaled by Ω_i^{-1}. The system size in the x direction is 128 and in the y direction is 256, normalized to ρ_s, the shown pictures are lower half of the simulation fields. The vertical axis indicates x-direction, and the horizontal axis indicates y-direction. The bottom line of each pictures corresponds to the separatrix.

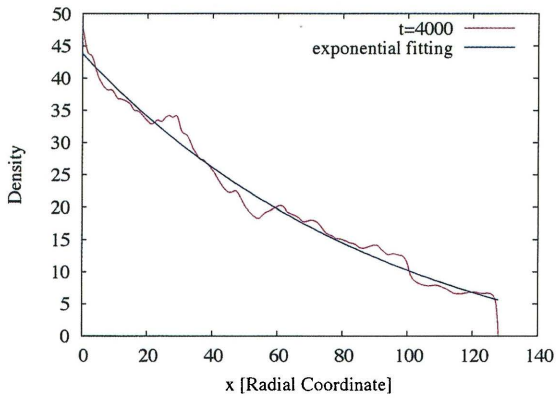

Fig. 27 Radial density profile of the $m = 0$ mode at $t = 4000$ and the exponential fitting curve to the profile. The vertical axis indicates x-direction, and the horizontal axis indicates density.

2. We confirmed the instabilities which play a dominant role during the blob propagation process are categorized by the blob size[8].
   (a) When the blob size is small, Kelvin-Helmholtz instabilities dominate the break-up of blobs.
   (b) When the blob size is large, the interchange modes dominate the break-up of blobs.
3. We investigate the effect of the density nonlinearity by solving the partially linearized model and the full nonlinear model. Comparison of these two shows that:
   (a) The density steepening effect is suppressed by the density nonlinearity due to the convective nonlinearity.
   (b) The density nonlinearity makes the blob propagation speed slow.
4. We compare the power spectra by the blob propagation simulations with the full nonlinear and the semi-nonlinear model. We conclude that the density nonlinearity in the continuity equation has a minor effect and does not contribute so much to the blob propagation in the SOL.
5. From the linear analysis of the SOL interchange mode, We confirm that:
   (a) The diffusion and the influx current into the divertor plate suppress the SOL interchange instability.
   (b) The strength of the curvature drift destabilizes the SOL interchange instability.
6. The nonlinear evolution of the SOL interchange mode at the separatrix is investigated. We found that:
   (a) The velocity shear accompanied with the gradient of the electrostatic potential plays an important role for the detachment events even if the field is strongly turbulent.
   (b) The simulation of the blob creation with the density source at the separatrix is demonstrated, that shows the "Rayleigh-Taylor fin-

ger" development, detach event, and strongly turbulent structure.

The intermittent transport in the SOL could be investigated using Hasegawa-Wakatani type model and its simulation results analysed with the statistical method[18]. This is the near future work. However, we can not reproduce 2nd SOL structure discussed in the introduction by this model. This is because the creation of 2nd SOL strongly depends on the source term itself, therefore, we need to couple with the plasma edge and the SOL, consistently. This is the long range task.

Acknowledgements

Firstly, I would like to thank Professor M. Yagi for a warm and heartful guidance during the course of my research. He has given me continuous encouragement and thought-provoking advice. I would like to appreciate Professor Sanae-I. Itoh for important suggestions and support. Special thanks to Dr. M. Azumi and Dr. T. Takizuka for useful discussions and instructive comments. I am grateful to Associate Professor S. Inagaki and Assistant Professor K. Ohsawa for precious advises.

Furthermore, I am indebted to Mr. S. Nishimura, Mr. S. Tokunaga, Mr. A. Froese, and Mr. T. Maruta for fruitful discussions. I am grateful to Ms. K. Asano and Ms. F. Yonaga, secretaries of Our laboratory, for their help on miscellaneous administrative works of my campus life.

The work is partly supported by the Grant-in-Aid for Specially-Promoted Research MEXT (16002005), by the Grant-in-Aid for Scientific Research of JSPS (16360459, 1936415) and by the collaboration programs of NIFS and of Research Institute for Applied Mechanics of Kyushu University.

Finally, I would like to express deep gratitude to my family for their support.

References

1) N. Ohno. *Journal of Plasma Fusion Research* **82**, 205 (2006).
2) M. V. Umansky, S. I. Krasheninnikov, B. LaBombard, and J. L. Terry. *Physics of Plasmas* **5**, 3373 (1998).
3) J. A. Boedo, D. Rudakov, R. Moyer, S. Krasheninnikov, D. Whyte, G. McKee, G. Tynan, M. Schaffer, P. Stangeby, P. West, S. Allen, T. Evans, R. Fonck, E. Hollmann, A. Leonard, A. Mahdavi, G. Porter, M. Tillack, and G. Antar. *Physics of Plasmas* **8**, 4826 (2001).
4) J. R. Myra, D. A. D'Ippolito, D. P. Stotler, S. J. Zweben, B. P. LeBlanc, J. E. Menard, R. J. Maqueda, and J. Boedo. *Physics of Plasmas* **13**, 092509 (2006).
5) R. J. Maqueda, G. A. Wurden, S. Zweben, L. Roquemore, H. Kugel, D. Johnson, S. Kaye, S. Sabbagh, and R. Maingi. *Review of Scientific Instruments*, **72** 931 (2001).
6) O. Grulke, J. L. Terry, B. LaBombard, and S. J. Zweben. *Physics of Plasmas* **13**, 012306 (2006).
7) J. A. Boedo, D. L. Rudakov, R. A. Moyer, G. R. McKee, R. J. Colchin, M. J. Schaffer, P. G. Stangeby, W. P. West, S. L. Allen, T. E. Evans, R. J. Fonck, E. M. Hollmann, S. Krasheninnikov, A. W. Leonard, W. Nevins, M. A. Mahdavi, G. D. Porter, G. R. Tynan, D. G. Whyte, and X. Xu. *Physics of Plasmas* **10**, 1670 (2003).
8) A. Y. Aydemir. *Physics of Plasmas* **12**, 062503 (2005).
9) O. E. Garcia, N. H. Bian, and W. Fundamenski. *Physics of Plasmas* **13**, 082309 (2006).
10) O. E. Garcia, N. H. Bian, V. Naulin, A. H. Nielsen, and J. Juul Rasmussen. *Physics of Plasmas* **12**, 090701 (2005).
11) G. Q. Yu and S. I. Krasheninnikov. *Physics of Plasmas* **10**, 4413 (2003).
12) D. A. D'Ippolito and J. R. Myra. *Physics of Plasmas* **10**, 4029 (2003).
13) N. Bian, S. Benkadda, J. -V. Paulsen, and O. E. Garcia. *Physics of Plasmas* **10**, 671 (2003).
14) D. A. Russell, J. R. Myra, D. A. D'Ippolito. *Physics of Plasmas* **14**, 102307 (2007).
15) D. Reiser. *Physics of Plasmas* **14**, 082314 (2007).
16) S.I. Krasheninnikov. *Physics Letters A* **283**, 368 (2001).
17) D. A. D'Ippolito, J. R. Myra, and S. I. Krasheninnikov. *Physics of Plasmas* **9**, 222 (2002).
18) P. Ghendrih, Y. Sarazin, G. Attuel, S. Benkadda, P. Beyer, G. Darmet, G. Falchetto, C. Figarella, X. Garbet, V. Grandgirard, M. Ottaviani. *Journal of Nuclear Materials* **337** 347 (2005).
19) A. Hasegawa, M. Wakatani *Physical Review Letters* **50** 682 (1983)
20) S. A. Orszag. *Physics of Fluids Supplement II* **12**, 250 (1969)
21) S. A. Orszag. *Journal of the Atmospheric Science* **27** 890 (1970)
22) E. Eliasen, B. Machenhauer, E. Rasmussen. *On a Numerical Method for Integration of the Hydrodynamical Equations with a Spectral Representation of the horizontal fields* Rep. No. 2 (1970)

Appendix

A1. Spectral and Pseudo-Spectral Method

In this thesis, we mainly use the pseudo-spectral code to solve model equations. In subsection 3.3.1, we have compared the spectral and the pseudo-spectral codes with each power spectra. In this appendix, we briefly explain how to solve a nonlinear equation using spectral and pseudo-spectral methods.

To explain both methods, we use the 1-dimensional nonlinear advection equation, as an example,

$$\frac{\partial u}{\partial t} + u\frac{\partial u}{\partial x} = 0, \tag{A1}$$

where the following conditions are assumed:

$$\text{Initial Condition:} \quad u(x,0) = f(x), \tag{A2}$$

$$\text{Boundary Condition:} \quad u(x,t) = u(x+2\pi,t). \tag{A3}$$

Expanding $u(x,t)$ in Eq. (A1) with Fourier series,

$$u(x,t) = \sum_{k=-N}^{N} \hat{u}_k(t)\, e^{ikx}, \tag{A4}$$

where N is the wave cut which determines the numerical resolution. Substituting Eq. (A4) into the L.H.S. of Eq. (A1), the residual R is given by

$$R(x,t) = \sum_{k=-N}^{N} \frac{\mathrm{d}\hat{u}_k}{\mathrm{d}t} e^{ikx} + \sum_{k=-N}^{N}\sum_{l=-N}^{N} il\hat{u}_l\hat{u}_k\delta e^{ikx}e^{ilx}. \tag{A5}$$

Multiplying the weighting function e^{-imx} to both sides, integrating 0 to 2π with x, and assuming the integral of the residual is 0, then we obtain the ordinary differential equation,

$$\frac{\mathrm{d}\hat{u}_m}{\mathrm{d}t} + \sum_{k=-N}^{N}\sum_{l=-N}^{N} il\hat{u}_l\hat{u}_k\delta_{k+l,m} = 0. \tag{A6}$$

Taking the Kronecker delta into account Eq. (A6) is expressed as

$$\frac{\mathrm{d}\hat{u}_m}{\mathrm{d}t} + \sum_{l=\max(-N,-N+m)}^{\min(N,N+m)} il\hat{u}_{m-l}\hat{u}_l = 0 \qquad (m=-N,\ldots,N), \tag{A7}$$

where the upper and lower limit of the summation on l is derived by taking account the range of k and l varies $-N \le k,l \le N$ and using the relation $\delta_{k+l,m} = 1$ when $k = m - l$.

For the spectral method, the nonlinear term in Eq. (A7) is evaluated in the Fourier and $O(N^2)$ operations are needed for the summation. However, the use of pseudo-spectral transform methods enables it to be evaluated in $O(N\log_2 N)$ operations. This technique was developed independently by Orszag[20,21] and Eliasen, Machenhauer and Rasmussen[22]:

1. Discrete inverse Fourier transforms of $\hat{u}_k$ and $ik\hat{u}_k$

$$u_j = \sum_{k=-N}^{N} \hat{u}_k e^{ikx_j}, \quad \left(\frac{\partial u}{\partial x}\right)_j = \sum_{k=-N}^{N} ik\hat{u}_k e^{ikx_j} \qquad (j=0,\ldots,J-1) \tag{A8}$$

2. estimation of the nonlinear term in the real space

$$F_j = \left(u\frac{\partial u}{\partial x}\right)_j = u_j\left(\frac{\partial u}{\partial x}\right)_j \qquad (j=0,\ldots,J-1) \tag{A9}$$

3. then discrete Fourier transform of F_j

$$\hat{F}_k = \frac{1}{J}\sum_{j=0}^{J-1} F_j e^{-ikx_j} \qquad (k=-N,\ldots,N) \tag{A10}$$